Title

Voxelwise Prediction of Recurrent High-Grade Glioma via Proximity Estimation–Coupled Multidimensional Support Vector Machine

Journal

International Journal of Radiation Oncology • Biology • Physics, 112(5)

ISSN

0360-3016

Authors

Lao, Yi
Ruan, Dan
Vassantachart, April
et al.

Publication Date

2022-04-01

DOI

10.1016/j.ijrobp.2021.12.153

Peer reviewed

HHS Public Access

Author manuscript

Int J Radiat Oncol Biol Phys. Author manuscript; available in PMC 2023 April 01.

Published in final edited form as:

Int J Radiat Oncol Biol Phys. 2022 April 01; 112(5): 1279–1287. doi:10.1016/j.ijrobp.2021.12.153.

Voxel-wise prediction of recurrent high grade glioma via proximity estimation coupled multi-dimensional SVM

Yi Lao, Ph.D.[1], **Dan Ruan, Ph.D.**[1], **April Vassantachart, M.D.**[2], **Zhaoyang Fan, Ph.D.**[3], **Jason C. Ye, M.D.**[2], **Eric L. Chang, M.D.**[2], **Robert Chin, M.D., Ph.D.**[1], **Tania Kaprealian, M.D**[1], **Gabriel Zada, M.D., M.S.**[4], **Mark S Shiroishi, M.D.**[3], **Ke Sheng, Ph.D.**[1,*], **Wensha Yang, Ph.D.**[2,*]

[1]Department of Radiation Oncology, University of California - Los Angeles, USA

[2]Department of Radiation Oncology, Keck School of Medicine of USC, Los Angeles, USA

[3]Department of Radiology, Keck School of Medicine of USC, Los Angeles, USA

[4]Department of Neurosurgery, Keck School of Medicine of USC, Los Angeles, USA

Abstract

Purposes: To provide early and localized glioblastoma (GBM) recurrence prediction, we introduce a novel post-surgery multi-parametric MR-based support vector machine (SVM) method coupling with stem cell niches (SCN) proximity estimation.

Methods: This study utilized post-surgery MRI scans ~2 months before clinically diagnosed recurrence from 50 patients with recurrent GBM. The main prediction pipeline consists of a proximity-based estimator to identify regions with high risks of recurrence (HRR), and an SVM classifier to provide voxel-wise prediction in HRR. The HRRs were estimated using the weighted sum of inverse distances to two possible origins of recurrence – SCN and tumor cavity. Subsequently, multi-parametric voxels (from T1, T1ce, FLAIR, T2, ADC) within the HRR were grouped into recurrent (warped from the clinical diagnosis) and non-recurrent subregions, and fed into the proximity estimation coupled SVM classifier - SVM_{PE}. The cohort was randomly divided into 40% and 60% for training and testing, respectively. The trained SVM_{PE} was then extrapolated to an earlier time point for earlier recurrence prediction. As an exploratory analysis, the SVM_{PE} predictive cluster sizes and the image intensities from the five MR sequences were compared across time to assess the progressive subclinical traces.

Results: On 2-month pre-recurrence MRIs from 30 test cohort patients, the SVM_{PE} classifier achieved a recall of 0.80, a precision of 0.69, an F1-score of 0.73, and an average boundary distance of 7.49 mm. Exploratory analysis at early time points showed spatially consistent but

The telephone number, and the e-mail address of the corresponding author: 323-865-3089 (o), Wensha.Yang@med.usc.edu, 310-267-8979 (o), ksheng@mednet.ucla.edu.

*equal last author contribution.

Research data are stored in an institutional repository and will be shared upon request to the corresponding author.

The authors declare no conflicts of interest.

significantly smaller subclinical clusters and significantly increased T1ce and ADC values over time.

Conclusion: We demonstrated a novel voxel-wise early prediction method, $SVM_{PE,}$ for GBM recurrence based on clinical follow-up MR scans. SVM_{PE} is promising in localizing subclinical traces of recurrence 2-month ahead of clinical diagnosis and may be used to guide more effective personalized early salvage therapy.

Keywords

GBM; SCN; Localized recurrence prediction; SVM

1 Introduction

Glioblastoma (GBM) is a deadly primary brain cancer that recurs in nearly all patients despite aggressive interventions, including maximal safe surgical resection, chemoradiotherapy, and tumor treating fields. Radiotherapy (RT), following surgery, offered improved survival and has long been an essential component of high-grade glioblastoma treatment [1–3]. However, RT ultimately fails to control GBM locally [4]. The unsatisfactory treatment outcome is partly because most GBMs are diagnosed in the advanced stage with tumor infiltration into the brain parenchyma that precludes a complete resection. The biological drivers of GBM resistance to treatment are not fully understood [5]. They are likely due to a combination of GBM's intrinsic radioresistance [6], its diffusely infiltratuve nature [7–8], and tumor stem cell niche [9–10]. Overcoming tumor radioresistance requires a high radiation dose, which is contraindicated by the need for a large margin and treatment volume to encompass the diffuse tumor and stem cell niches. The predicament is further complicated because current GBM diagnosis and prognosis methods are not suited to precisely map the disease infiltration for recurrence prediction and personalized initial treatment target volume definition.

Cancergenesis analyses on tumor tissue provide a pathological snapshot of tumor cells and allow for patient profiling at the genomic and proteomic levels. However, while pathological subtyping dictates tumor aggressiveness and prognosis, it yields limited insights on the location of the recurrence for image-guided RT planning. A few radiologic efforts, including functional imaging (i.e. ^{18}F-fluoro-ethyl-tyrosine positron emission tomography (^{18}F-FET PET)) [11], diffusion MRI [12], CEST [13], and MR spectroscopy [14], and the new image postprocessing method [15] (i.e. radiomics analysis in peritumoral edema), have been made to predict GBM recurrence. Advanced PET and MR images taken before RT may reveal the tumor volumes inadequately covered by the RT field, but they suffer from two limitations. First, a sufficient number of cancer cells are needed to generate the imaging signal-to-noise ratio for detection. These modalities are unable to detect subclinical cancer infiltration. Second, the snapshot images at a single time may not reflect the dynamic progression of disease due to local and distal factors. Radiomics extracted features in the edema to help identify recurrence adjacent to initial tumors. However, this method cannot identify the substantial portion of the recurrence distal to the initial location. Alternatively, algorithms probing into the cell of origin and enabling early and localized detection of subclinical recurrence may offer the opportunity to treat the recurrence volume at an earlier

time and to a greater radiation dose. Emerging evidence has associated the pathogenesis of GBM recurrence with the involvement of stem cell niche (SCN), providing a potential new direction for prediction [16–21]. Aiming to clarify the weak or controversial correlation between SCN and patient survival [22], a comprehensive inverse geometrical metric was developed, which revealed the statistical significance of SCN involvement in GBM recurrence and patient survival [23]. Although increasing SCN-directed studies succeeded in progression and survival risk stratification, they did not directly translate into localized recurrence prediction for salvage RT planning.

This study introduces a quantitative proximity-based support vector machine (SVM_{PE}) for localized recurrence prediction. We hypothesize that peritumoral infiltration and SCN migration collectively contribute to the GBM recurrence and an integrated proximity estimation to both locations provides comprehensive profiling of regional recurrence risk. Within high-risk regions (HRR) narrowed down by proximity estimation, we trained an SVM model for voxel-wise recurrence prediction on postoperative follow-up MRIs. We evaluated the performance of SVM_{PE} on MR scans obtained two months before recurrence and then extrapolated the model on scans acquired at earlier time points for further advanced recurrence localization.

2 Methods

2.1 Data and preprocessing

Multi-parametric MRI scans of 50 patients with recurrent GBM were retrospectively solicited from multiple databases: 9 patients from the publicly available Cancer Imaging Archive (TCIA) dataset [24] and 41 patients from two institutional databases (USC IRB #HS-19–00888 and UCLA IRB#12–001882, aged from 18–73 years (50.5 ± 13.4 years), 10 female and 31 male). Patients were selected according to the following criteria: 1) had surgical resection at initial diagnosis; 2) had clinically diagnosed recurrence; 3) received at least one follow-up MR scans within three months ahead of clinically diagnosed recurrence, as well as one diagnostic MR scan at the time of recurrence. 4) follow-up scans were taken at least one week after surgery and three months post-RT (or shown no signs of pseudo-progression). 5) MR scans consisting of 5 standard clinical MR sequences as detailed below. Additional eligible follow-up scans from 25 of the 50 subjects were included in the study for exploratory analyses. Dataset consisted of multicenter, multi-vendor MR scans with field strengths of 1.5T or 3T, and slice-thickness from 1 – 6mm. The five standard clinical sequences for each scan set included T1-weighted (T1), T1 contrast-enhanced (T1ce), T2-weighted (T2), T2 Fluid-Attenuated Inversion Recovery (FLAIR), and diffusion-weighted echo-planar imaging sequence derived apparent diffusion coefficient (ADC) map. Primary tumor volumes, defined as resection cavities in this study, and recurrence volumes were segmented by an experienced radiologist mainly on T1ce images and FLAIR, with other sequences for complimentary assessments. SCN zones, including bilateral subventricular zone extending from the wall of each lateral ventricle and subgranular zone residing at the interface between the hilus and the granular layer of each hippocampus, were manually delineated on a common T1-weighted Montreal Neurological Institute (MNI) template

[23,25]. The intra-rater variability Dice score of SCN identification was 0.95, by one radiation oncology trainee spanning two weeks.

To minimize the individual variance of brain size and ventricular anatomy and thus facilitate subsequent population-based statistical analysis, we performed the following image processing. Each MRI scan was preprocessed for skull stripping, N3 bias correction, and linear alignment to the corresponding first pre-recur T1 scan [26–28]. All MR scans were resampled into the isotropic 1×1×1 mm^3 resolution, and deformably registered to the MNI space using pathology adaptive deformable registration in advanced normalization tools (ANTs) [25, 29]. Specifically, the MNI template was deformably aligned to each T1 MR scan using the state-of-art Symmetric Normalization diffeomorphic registration. The noncorresponding tumor regions (i.e., cavities and recurrences) were excluded from the registration cost function. The resultant inverse transformations were then propagated onto other MR sequences and primary and recurrent tumor volumes [26, 28].

2.2 Overall pipeline

A diagram of the training scheme of the proximity-based SVM classifier, SVM_{PE}, is shown in Figure 1. The classifier consists of two main steps: proximity-based calculation to identify regions with a high risk of recurrence and SVM classifier training to leverage voxel-wise prediction in the high-risk areas. The SVM_{PE} training was conducted in the follow-up MRI scans acquired immediately before clinically diagnosed recurrence (Figure 1(ii)) when subclinical recurrence likely had started but was not discernible from clinical MRIs. The whole cohort was randomly divided into a 40% (20 subjects) training cohort and a 60% (30 subjects) testing cohort. The involved data centers were proportionally balanced for both cohorts to reduce institutional variations. As an exploratory investigation (Figure 1(ii)), the trained SVM_{PE} classifier was then applied on the scans acquired one time-point earlier (on average four months before recurrence) to test the feasibility of further earlier recurrence prediction.

2.3 Proximity estimation and High-risk region-of-interest (HRR)

We initially estimated the recurrence risks based on proximity to two hypothesized origins, SCN [23, 30–31] and original tumor (P_T) [32–33], respectively. The degree of proximity to the SCN (P_S) is estimated based on the normalized sum of inverse distances:

$$P_S(x) = \begin{cases} \dfrac{\mathscr{D}(x) - \mathscr{D}_{min}}{\mathscr{D}_{max} - \mathscr{D}_{min}}, \ if\ x \notin S \\ 1, \ if\ x \in S \end{cases} \tag{1}$$

where

$$\mathscr{D}(x) = \sum_{i=1}^{N} \frac{1}{d(x, s_i)^2} \tag{2}$$

S_i *with* $i \in [1, N]$ denotes an observation in SCNs, with x being an interpolated voxel in the region of interest. $d(x, V_i)$ represents the squared Euclidean distance between x and a given

observation in S. $\mathscr{D}_{max}$ and $\mathscr{D}_{min}$ are the maximum and minimum inversed distances $\mathscr{D}(x)$ within S for a given subject, respectively.

Similarly, proximity estimation, P_T, to the original tumor T_i *with* $i \in [1, M]$, is defined as:

$$P_T(x) = \begin{cases} \dfrac{\mathscr{D}(x) - \mathscr{D}_{min}}{\mathscr{D}_{max} - \mathscr{D}_{min}}, \ if \ x \notin T \\ 1, \ if \ x \in T \end{cases} \tag{3}$$

The high-risk region-of-interest (HRR) was estimated by the aggregated recurrence risks from the SCN and the primary tumor through a combination of P_S and P_T, as:

$$\alpha P_T + P_S \geq c \tag{4}$$

where α adjusts the weighting between P_T and P_S, and c thresholds the aggregated risk to create a final ROI. α and c were selected using grid search to maximize the inclusion of recurrence through a weighted mean of sensitivity and precision (maximize[*Recall**2 + *Precision*, (*ROI*, *Recurrence*)]) on the training set. Figure 2 shows 3D renderings of calculated HRRs in 4 example subjects.

2.4 SVM classifier and performance evaluation

A radial basis function (RBF) kernel SVM classifier [34–35] was used to isolate recurrent subregions in previously defined HRRs further. Specifically, multi-dimensional voxels (T1, T1ce, FLAIR, T2, ADC) within HRRs were fed into SVM, with recurrent subregions (green in Figure 3) being class 1 and non-recurrent subregions excluding original tumors (blue in Figure 3) being class 2. We normalized all MR scans using the z-score method with a center of 0 and a standard deviation of 1 [36] to reduce the intensity variations due to heterogeneous acquisition protocols and scanners. To maintain a balance between the two training classes, we limited non-recurrence inputs to 30,000 voxels, randomly selected from the HRR, for each subject. An RBF kernel scale $\gamma = 2$ and a box-constraint $C = 100$ were selected based on the performance from a validation subset of 10 subjects from the training cohort. Due to the nature of voxel-wise prediction, the original outputs from SVM may be geometrically unrealistic (i.e., noisy and sparse), which can be alleviated by morphological postprocessing [37]. Specifically, a Gaussian kernel was applied on the binarized raw predictions from SVM, followed by distance-based clustering with minimal Euclidean distance of 1 voxel, to remove small, isolated regions whose sizes are smaller in a cutoff percentage. Kernel sizes 3×3, 5×5, 7×7, and cutoff values of 30%, 50%, 70% were investigated, and the 5×5 kernel and 50% cutoff were selected based on the performance of the training cohort.

The SVM_{PE} model was first evaluated by comparing the binary classification outputs with the warped recurrence and the non-recurrence region within the HRRs, shown in Figure 1(i) as the green and light blue regions, respectively. Specifically, the performance was assessed using recall (a measurement of the classification sensitivity), precision (a measurement of

the positive prediction rate), and F1 score (the harmonic mean of precision and recall). The mathematical definitions are:

$$\text{Recall} = \frac{\text{true positive}}{\text{true positive} + \text{false negative}} \tag{5}$$

$$\text{Precision} = \frac{\text{true positive}}{\text{true positive} + \text{false positive}} \tag{6}$$

$$\text{F1} = 2 * \frac{\text{Recall} * \text{Precision}}{\text{Recall} + \text{Precision}} \tag{7}$$

In addition, while the warped recurring ROI affords a higher probability of later recurrence, its specific boundaries do not necessarily dictate the demarcation of the subclinical traces. As a result, we also calculated the average boundary distance (ABD), a metric assessing the degree of spatial disagreement between the 3D surfaces, as a more generalized evaluation of the' relevance' of predictions [38–39]. Specifically, given a surface vertex set $S_P = \{S_{Pi}, i \in [1, N_{S_P}]\}$, on the 3D surface generated from a binarized prediction, and the corresponding surface vertex set $S_R = \{S_{Rj}, j \in [1, N_{S_R}]\}$, generated from the recurring ROI, ABD was obtained using:

$$ABD = \frac{1}{N_{S_P} + N_{S_R}} \left(\sum_{i=1}^{N_{S_P}} \min_{S_{Rj} \in S_R} d(S_{Pi}, S_{Rj}) + \sum_{j=1}^{N_{S_R}} \min_{S_{Pi} \in S_P} d(S_{Rj}, S_{Pi}) \right) \tag{8}$$

Where $d(S_{Pi}, S_{Rj})$ represents the Euclidean distance between a surface vertex S_{Pi} in the prediction and a surface vertex S_{Rj} in the corresponding recurring ROI, thus the ABD has a unit of mm.

2.5 Extrapolation to longitudinal data

To test the feasibility of early subclinical tumor tracking at a further upstream time point, we applied the trained SVM_{PE} model on the 25 subjects with additional MRI scans on average four months (±1.3 months) before recurrence (t-2 time point in Figure 1(ii), orange icons). Pairwise student t-tests were used to compare the SVM_{PE} predictive cluster sizes from two pre-recur (t-1 and t-2) time points to test detectable subclinical progressions.

As an exploratory analysis, to investigate the underline subclinical anatomical changes, normalized imaging intensities from the 5 MR sequences (T1, T1ce, T2, FLAIR, ADC) were extracted from both pre-recur time points, using the warped recurrence regions as region-of-interests. Pairwise student t-tests were then performed between the two pre-recur time-points in terms of the mean of the five extracted imaging indices.

3 Results

3.1 Two-month advanced predictions

To maximize the inclusion of recurrence in HRR, as stated in section 2.3, $\alpha = 3.5$ and $c = 0.9$ were selected based on the training set. Metrics assessing the performance of SVM_{PE} for both the training and testing cohorts on 2-month pre-recur MR scans are summarized in Table. 1. Performance on the training cohort were obtained with 10-fold cross-validation. Compared to binarized recurring and non-recurring ROIs within HRR, SVM_{PE} resulted in averaged predictive recall of 0.81 and 80, averaged precision of 0.68 and 0.69, and averaged F1 score of 0.73 and 0.73 for the training and the testing cohort, respectively. Group-wise t-tests revealed no significant performance differences between the two cohorts. Similar performance between the two cohorts was also confirmed by the distance-based metric ABD, indicating good generalization of SVM_{PE} onto the test set. Figure 3 shows SVM_{PE} predictions for two example subjects and the corresponding 5 MR scans in the same view. For both subjects, the demarcation of T1 contrast-enhanced regions greatly underestimated the regions with later recurrence (red, warped, and overlaid on T1ce images). At the same time, intensity enhancements in T2, FLAIR, or ADC maps were less specific in revealing subclinical traces. In contrast, the SVM_{PE} predictions corresponded well with later clinical diagnosed recurrence in both cases.

3.2 Longitudinal subclinical changes

Results of longitudinal predictions and intensity comparisons across time are shown in Figures 4 and 5. As we can see from Figure 4, compared to the prediction from the immediate pre-recur (2 months prior) time point, the predicted clusters from 4-month apart were located in similar locations but generally smaller in size. This pattern can be evidently visualized in Figure 5(a), where the majority of the subjects presented an enlargement in subclinical regions as approaching the recurrence. The pairwise t-test revealed a significant size difference between the two time points, with $p = 0.004$. Besides, comparisons of image indices on T1ce and ADC maps between these two time points revealed significant intensity enhancements over time, while comparisons on T1, T2, and FLAIR signals failed to reach group-wise significance.

4 Discussion

In the study, we showed the feasibility of predicting the subclinical recurrence locations based on post-RT longitudinal MR images and biology-driven geometrical features. The novel therapeutic implication and voxel-wise recurrence prediction method are distinctly different from existing efforts of recurrence prediction.

Existing research for recurrence prediction is intended for modification of the initial treatment volume. For this reason, the studies are focused on the pretreatment images. Peritumoral infiltration of tumor cells has been considered one of the primary sources of GBM recurrence, with edema areas having the highest probability of infiltration [32]. Based on this assumption, Rathore et al. performed a radiomics analysis on peritumoral edema using pre-operative traditional and perfusion MRI and achieved decent prediction in local

recurrence [15]. Nonetheless, although pre-operative local infiltration may contribute to later recurrence, especially the ones that recurred within a few months following treatment, it is not the only resource of recurrences, as a substantial portion of the recurrence spread into regions distant (> 2cm) from the initial location [30]. Without the peritumoral assumption, Harat et al. prospectively investigated the possibility of using 18F-fluoro-ethyl-tyrosine (18F-FET) PET to predict the recurrence location [11], as the MR-defined target volume insufficiently covered the PET avid volume. Although the FET avid volumes showed improved overlap with the recurrent volumes, they suffer from two limitations. First, the number of cells (i.e., 10E6 cells) required to produce sufficient PET signals prevents it from detecting microscopic infiltration [40]. Second, the pretreatment snapshot cannot capture the morphological and pathological alterations during and after initial treatments [41]. Other advanced imaging methods for recurrence prediction, including diffusion MRI [12], CEST [13], and MRS [14], suffer from similar limitations. Unlike these studies aiming to modify the *initial* treatment volume, we designed our study to improve the *recurrent* treatment by fully utilizing the longitudinal imaging information for patients under frequent imaging surveillance following their initial treatment. Early GBM recurrence prediction provides a second avenue for the personalized therapeutic design, which may be implemented at an earlier time point to maximally delay *recurrent* disease progression with safe radiation dose escalation to a smaller target volume.

Regarding the prediction method, beyond what can be captured in images of the tumor and its periphery, recent cancerogenesis analyses have suggested the role of SCN in the pathogenesis of GBM recurrence, providing a new direction for localizing subclinical trace of recurrence [16]. For example, recurrence has been demonstrated to have a higher tendency to spread closer to SCN, regardless of the initial tumor location [3, 23, 42]. However, the radiologic definition of SCN is inconsistent among studies [3,18,42]. The proximity to SCN has been ineffectively characterized by the semi-quantitative measurements adopted by most of the SCN derived studies. For the same reason, the role of SCN in GBM formation and progression has not been translated into localized voxel-level recurrence prediction.

Our localized GBM recurrence prediction model is based on the interplaying contribution of peritumoral infiltration and SCN migration, thus providing comprehensive profiling of regional recurrence risk. On clinical follow-up MRI, the proximity to the SCN and primary tumor was quantitatively characterized using inverse distance mapping. The GBM localization was consecutively narrowed down by integrated proximity estimation and voxel-wise SVM classification. On 2-month pre-recur scans, our model successfully delineates subclinical pathologies that are consistent in the location with later radiologically confirmed recurrences, albeit not clearly defined from either single MR sequence (Figure 3). The performance comparison between the training and testing sets suggests the good generalizability of the SVM_{PE} model (Table 1). Since our SVM model is based on standard clinical MR sequences, the proposed method will be easily implemented as an add-on to current clinical practice without additional sophisticated imaging scans.

In extrapolation analysis to an earlier time point (4 months before recurrence), the trained SVM_{PE} model predicted significantly smaller cluster size in similar locations, indicating

a potential trend of subclinical progression and the possibility of using SVM_{PE} for more advanced subclinical trace localization. The existence of progressive subclinical changes is further evidenced by the exploratory analysis of MR signals between two pre-recur time points (Figure 5). In particular, as the current gold standard of clinical tumor recurrence diagnosis, T1ce signals presented a small but significant increase from 4 to 2 months before recurrence. On top of it, the considerable rise of ADC values, which are inversely proportional to tumor cellularity, may indicate a decreased microstructural neurite density [43]. These are in line with the findings from Jin et al., where neurite density loss, represented by changes in fractional anisotropy and neurite density indices, was also observed at two months before recurrence on 30 GBM patients [44]. Our novel method captures the SCN and MR information more comprehensively for early recurrent location prediction.

We evaluated our model using both volume and average boundary distance agreement between the prediction and the actual recurrence. The performance indicates the ability to locate future recurrence, but the factor of tumor progression between the time points needs to be considered. A lower recall is expected, particularly for further upstream analysis where the predicted tumor volume is smaller than recurrence at a later time point. Besides performance evaluation, the distance agreement can help define the target volume in radiotherapy planning.

Our study has several notable limitations. First, the use of generic-lesion-based registration and the MNI template for brain alignment. Although being the current state-of-the-art method for pathological brain registration, lesion-based ANTs cannot fully adapt to specific challenges in GBM brain alignment, i.e., mapping excessive edema that constantly changes across the follow-up period. On top of it, the MNI brain template based on healthy subjects inadequately captures anatomy characteristics in GBM brains, such as degenerated white matter and enlarged lateral ventricles. These differences may introduce further errors in the manual identification of SCN, especially the areas in ventricular vicinity. In the future, an advanced pathological-adaptive registration algorithm and a brain template specific to the GBM population are needed to facilitate more accurate intra- and inter-patient image alignment [41]. Second, the generation and testing of the SVM_{PE} were based on a limited dataset without screening on confounding factors, such as genomic subtypes initial tumor sizes, and treatment regimens. The moderate standard deviation on prediction performance (Table. 1) may suggest a non-negligible population heterogeneity, possibly due to the underlying divergent recurrent patterns and speeds. Whether the performance differences dictate pathological or therapeutic subtypes and whether the current model can be further refined according to these subtypes need to be explored in a larger dataset. Third, the MR datasets were obtained through multi-scanners on multi-sites. While normalized using a standard protocol [36], the remarkable variations in tissue intensity due to acquisition protocol and scanner differences can not be disregarded. In the future, we will prospectively acquire quantitative MR images to minimize the impact of inter-scan variations on SVM predictions [45]. Fourth, the SVM_{PE} model was trained and tested on scans sparing the 3-month time window after RT to avoid the complications of pseudo-progression. However, pseudo-progression is commonly seen in 20–30% of patients following RT and remains a critical factor in interfering with clinical decisions [43, 46]. Therefore, although the current

model yield localized early recurrence prediction two months before clinical diagnosis, an advanced prediction model capable of identifying the distinctive trace of recurrence over concurrent treatment-related pseudo-progression are needed in the future, to achieve clinically robust recurrence prediction and monitoring in the entire clinical course after treatment [47].

5 Conclusion

In the presented study, we introduced a novel voxel-wise early prediction method for brain GBM recurrence based on clinical follow-up MR scans using an SCN proximity estimation coupled SVM framework- SVM_{PE}. The result shows promise in localizing subclinical traces of recurrence 2-month ahead of clinical diagnosis. The proposed method could be easily implemented as an add-on to current clinical practice without additional imaging scans. The derived voxel-wise prediction may serve as a target volume for advanced dosimetric planning that maximally includes invisible infiltrative cancer cells in the recurrent treatment at an earlier time to delay cancer progression.

Acknowledgments

This research is supported by the 2020 AAPM Research Seed Funding Grant.

References

[1]. Linde Myra E, Brahm Cyrillo G, Witt Hamer Philip C, et al. Treatment outcome of patients with recurrent glioblastoma multiforme: a retrospective multicenter analysis. J. Neuro-Oncol 2017;135:183–192.

[2]. Walker Michael D, Green Sylvan B, Byar David P, et al. Randomized comparisons of radiotherapy and nitrosoureas for the treatment of malignant glioma after surgery. N Engl J Med. 1980;303:1323–1329. [PubMed: 7001230]

[3]. Ron Batash, Noam Asna, Pamela Schaffer, Nicole Francis, Moshe Schaffer. Glioblastoma multiforme, diagnosis and treatment; recent literature review. Curr. Med. Chem 2017;24:3002–3009. [PubMed: 28521700]

[4]. Justin Mann, Rohan Ramakrishna, Rajiv Magge, Gabriella Wernicke A. Advances in radiotherapy for glioblastoma. Front Neurol. 2018;8:748. [PubMed: 29379468]

[5]. Yousuf Ali Md, Oliva Claudia R, Noman Abu Shadat M, et al. Radioresistance in Glioblastoma and the Development of Radiosensitizers. Cancers. 2020;12:2511.

[6]. Mariella Mannino, Chalmers Anthony J. Radioresistance of glioma stem cells: intrinsic characteristic or property of the ‘microenvironment-stem cell unit’? Mol. Oncol 2011;5:374–386. [PubMed: 21659010]

[7]. Jana Lipková, Panagiotis Angelikopoulos, Stephen Wu, et al. Personalized radiotherapy Design for Glioblastoma: integrating mathematical tumor models, multimodal scans, and Bayesian inference. IEEE trans on medical imaging. 2019;38:1875–1884. [PubMed: 30835219]

[8]. Syreeta DeCordova, Abhishek Shastri, Tsolaki Anthony G, et al. Molecular heterogeneity and immunosuppressive microenvironment in Glioblastoma. Front. immunol 2020;11:1402. [PubMed: 32765498]

[9]. Silver Daniel J, Lathia Justin D. Revealing the glioma cancer stem cell interactome, one niche at a time. J. Pathol 2018;244:260–264. [PubMed: 29282720]

[10]. Tejpal Gupta, Vimoj Nair, Nojin Paul Siji, et al. Can irradiation of potential cancer stem-cell niche in the subventricular zone influence survival in patients with newly diagnosed glioblastoma? J. Neuro-Oncol 2012;109:195–203.

[11]. Maciej Harat, Bogdan MaŃkowski, Roman Makarewicz. Pre-irradiation tumour volumes defined by MRI and dual time-point FET-PET for the prediction of glioblastoma multiforme recurrence: a prospective study. Radiother Oncol. 2016;120:241–247. [PubMed: 27378734]

[12]. Wahl Daniel R, Kim Michelle M, Aryal Madhava P, et al. Combining perfusion and high B-value diffusion MRI to inform prognosis and predict failure patterns in glioblastoma. Int. J. Radiat. Oncol. Biol. Phys 2018;102:757–764. [PubMed: 29980414]

[13]. Chan Rachel W, Hanbo Chen, Sten Myrehaug, et al. Quantitative CEST and MT at 1.5 T for monitoring treatment response in glioblastoma: early and late tumor progression during chemoradiation. J. Neuro-Oncol 2021;151:267–278.

[14]. Cordova James S, Shu Hui-Kuo G, Zhongxing Liang, et al. Whole-brain spectroscopic MRI biomarkers identify infiltrating margins in glioblastoma patients. Neuro Oncol. 2016;18:1180–1189. [PubMed: 26984746]

[15]. Saima Rathore, Hamed Akbari, Jimit Doshi, et al. Radiomic signature of infiltration in peritumoral edema predicts subsequent recurrence in glioblastoma: implications for personalized radiotherapy planning. J. Med. Imaging 2018;5:021219.

[16]. Christine Altmann, Stefanie Keller, Schmidt Mirko HH. The role of SVZ stem cells in glioblastoma. Cancers. 2019;11:448.

[17]. Arnaud Lombard, Marina Digregorio, Clément Delcamp, Bernard Rogister, Caroline Piette, Natacha Coppieters. The subventricular zone, a hideout for adult and pediatric high-grade glioma stem cells. Front Oncol. 2020;10. [PubMed: 32047721]

[18]. Percy Lee, Wietse Eppinga, Frank Lagerwaard, et al. Evaluation of high ipsilateral subventricular zone radiation therapy dose in glioblastoma: a pooled analysis. Int. J. Radiat. Oncol. Biol. Phys 2013;86:609–615. [PubMed: 23462418]

[19]. Patrick Evers, Lee Percy P, John DeMarco, et al. Irradiation of the potential cancer stem cell niches in the adult brain improves progression-free survival of patients with malignant glioma. BMC cancer. 2010;10:1–7. [PubMed: 20047689]

[20]. Tejpal Gupta, Vimoj Nair, Rakesh Jalali. Stem cell niche irradiation in glioblastoma: providing a ray of hope? CNS oncol. 2014;3:367–376. [PubMed: 25363009]

[21]. Vivian Capilla-Gonzalez, Bonsu Janice M, Redmond Kristin J, Manuel Garcia-Verdugo Jose, Quiñones-Hinojosa Alfredo. Implications of irradiating the subventricular zone stem cell niche. Stem Cell Res. 2016;16:387–396. [PubMed: 26921873]

[22]. Mistry Akshitkumar M, Nishit Mummareddy, Sanjana Salwi, Davis Larry T, Ihrie Rebecca A. Glioblastoma Distance From the Subventricular Neural Stem Cell Niche Does Not Correlate With Survival. Front Oncol. 2020;10:2843.

[23]. Yi Lao, Victoria Yu, Anthony Pham, et al. Quantitative characterization of tumor proximity to stem cell niches: implications on recurrence and survival in GBM patients. Int. J. Radiat. Oncol. Biol. Phys. In Press, Available online 16 February 2021.

[24]. Schmainda KM Prah M Data from Brain-Tumor-Progression. The Cancer Imaging Archive. 10.7937/K9/TCIA.2018.15quzvnb. 2018.

[25]. GŘnther Grabner, Janke Andrew L, Budge Marc M, David Smith, Jens Pruessner, Louis Collins D. Symmetric atlasing and model based segmentation: an application to the hippocampus in older adults. MICCAI. 2006;58–66.

[26]. Shattuck David W, Leahy Richard M. BrainSuite: an automated cortical surface identification tool. Med Image Anal. 2002;6:129–142. [PubMed: 12045000]

[27]. Tustison Nicholas J, Avants Brian B, Cook Philip A, et al. N4ITK: improved N3 bias correction. IEEE trans on medical imaging. 2010;29:1310–1320. [PubMed: 20378467]

[28]. Mark Jenkinson, Beckmann Christian F, Behrens Timothy EJ, Woolrich Mark W, Smith Stephen M. FSL. Neuroimage. 2012;62:782–790. [PubMed: 21979382]

[29]. Avants Brian B, Tustison Nicholas J, Gang Song, Cook Philip A, Arno Klein, Gee James C. A reproducible evaluation of ANTs similarity metric performance in brain image registration. Neuroimage. 2011;54:2033–2044. [PubMed: 20851191]

[30]. Sebastian Adeberg, Laila König, Tilman Bostel, et al. Glioblastoma recurrence patterns after radiation therapy with regard to the subventricular zone. Int. J. Radiat. Oncol. Biol. Phys 2014;90:886–893. [PubMed: 25220720]

[31]. Linda Chen, Chaichana Kaisorn L, Lawrence Kleinberg, Xiaobu Ye, Alfredo Quinones-Hinojosa, Kristin Redmond. Glioblastoma recurrence patterns near neural stem cell regions Radiother Oncol. 2015;116:294–300. [PubMed: 26276527]

[32]. Takahiro Yamahara, Yoshihiro Numa, Tetsuya Oishi, et al. Morphological and flow cytometric analysis of cell infiltration in glioblastoma: a comparison of autopsy brain and neuroimaging. Brain Tumor Pathol. 2010;27:81–87. [PubMed: 21046309]

[33]. Grabowski Matthew M, Recinos Pablo F, Nowacki Amy S, et al. Residual tumor volume versus extent of resection: predictors of survival after surgery for glioblastoma. J Neurosurg. 2014;121:1115–1123. [PubMed: 25192475]

[34]. Nello Cristianini, John Shawe-Taylor, others. An introduction to support vector machines and other kernel-based learning methods. Cambridge university press. 2000.

[35]. John Shawe-Taylor, Nello Cristianini, others. Kernel methods for pattern analysis. Cambridge university press. 2004.

[36]. Xiaofei Sun, Lin Shi, Yishan Luo, et al. Histogram-based normalization technique on human brain magnetic resonance images from different acquisitions. Biomed. Eng. Online 2015;14:1–17. [PubMed: 25564100]

[37]. Jie Wei. Shape indexing and recognition based on regional analysis. IEEE trans on multimedia. 2007;9:1049–1061.

[38]. Aziz Taha Abdel, Allan Hanbury. Metrics for evaluating 3D medical image segmentation: analysis, selection, and tool. BMC Med. Imaging 2015;15:1–28. [PubMed: 25645550]

[39]. Litjens Geert, Toth Robert, van de Ven Wendy, Hoeks Caroline, Kerkstra Sjoerd, van Ginneken Bram, Vincent Graham et al. Evaluation of prostate segmentation algorithms for MRI: the PROMISE12 challenge. Med. Image Anal 2014;18(2): 359–373. [PubMed: 24418598]

[40]. Fischer Barbara M., Minna WB Olsen Carsten D. Ley, Klausen Thomas L., Mortensen Jann, Liselotte Højgaard, and Paul EG Kristjansen. How few cancer cells can be detected by positron emission tomography? A frequent question addressed by an in vitro study. Eur J Nucl Med Mol Imaging. 2006;33(6): 697–702. [PubMed: 16612588]

[41]. Yi Lao, Victoria Yu, Eric Chang, Wensha Yang, Ke Sheng. Deformable alignment of longitudinal postoperative brain GBM scans using deep learning. Medical Imaging 2020: Image Processing. 11313:113130O.

[42]. Sebastian Adeberg, Tilman Bostel, Laila König, Thomas Welzel, Juergen Debus, Combs Stephanie E. A comparison of long-term survivors and short-term survivors with glioblastoma, subventricular zone involvement: a predictive factor for survival? Radiat Oncol. 2014;9:95. [PubMed: 24758192]

[43]. Marta Drake-Pérez, Jose Boto, Aikaterini Fitsiori, Karl Lovblad, Isabel Vargas Maria. Clinical applications of diffusion weighted imaging. Neuroradiol Insights Imaging. 2018;9:535–547.

[44]. Yan Jin, Randall James W, Hesham Elhalawani, et al. Detection of Glioblastoma subclinical recurrence using serial diffusion tensor imaging. Cancers. 2020;12:568.

[45]. Shinohara Russell T, Sweeney Elizabeth M, Jeff Goldsmith, et al. Statistical normalization techniques for magnetic resonance imaging. NeuroImage Clin. 2014;6:9–19. [PubMed: 25379412]

[46]. Young Robert J, Ajay Gupta, Shah Akash D, et al. MRI perfusion in determining pseudoprogression in patients with glioblastoma. Clin Imaging. 2013;37:41–49. [PubMed: 23151413]

[47]. Thust Stefanie C, Van Den Bent Martin J, Marion Smits. Pseudoprogression of brain tumors. J. Magn. Reson. Imaging 2018;48:571–589.

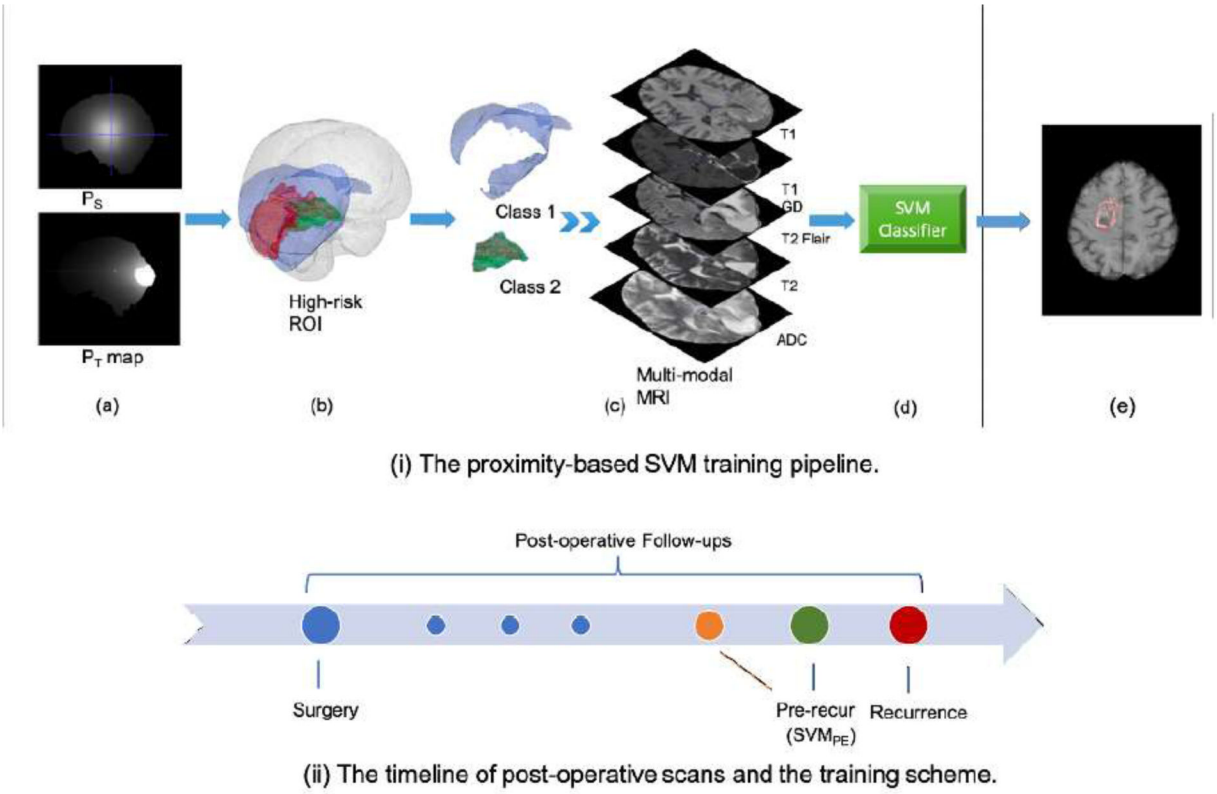

Figure 1:

Diagram of the proximity-based SVM training pipeline (i) and the timeline of postoperative scans and the training scheme (ii). In subplot (i): (a) Generation of proximity maps to stem cell zones (P_S) and the original tumor (P_T). (b) Calculation of high-risk region-of-interest (HRR) based on (P_S) and (P_T). (c) Using non-recurrence and recurrence subregions within HRR for feature extraction on multi-parametric MRIs. (d) Training a nonlinear multi-dimensional SVM_{PE} using the extracted voxels. (e) The expected output of voxel-wise recurrence prediction. In subplot (ii), the SVM classifier was trained using MRI scans acquired immediately before clinically diagnosed recurrence (green icon, on average 2-month apart. Named as t-1 time point, t being the recurrence time.). The trained classifier was then tested on the further upstream follow-up scan (orange icons, on average four months before recurrence. Named as t-2 time point.) as an exploratory analysis.

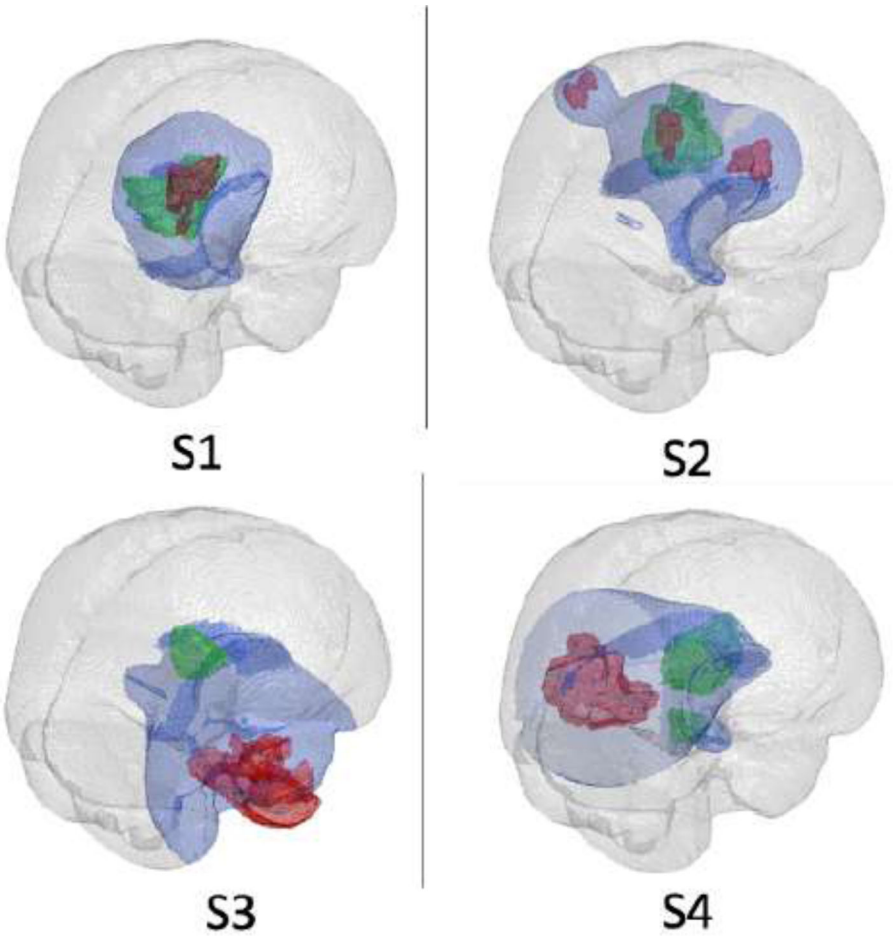

Figure 2:
3D rendering of the SCN proximity estimated HRR from step 1 for 4 example subjects. The HRRs (light blue) reflect patient-specific initial tumor location (red) and SCN proximity and effectively cover the regions with later recurrence (green), especially for patients with distal recurrences (S3 and S4.).

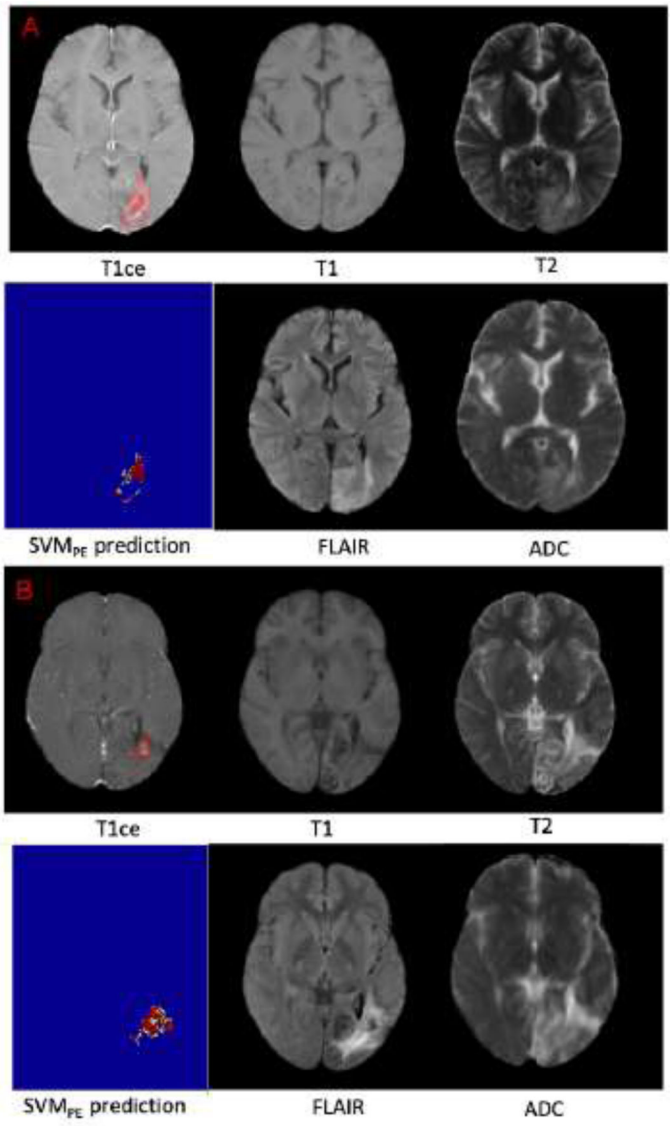

Figure 3:

Visualization of voxel-wise prediction results from SVM_{PE} for two subjects from the testing cohort. Subject A demonstrates a good prediction (ABD = 1.47 mm), and subject B exemplifies a typical prediction (ABD = 8.88 mm). For both patients, the pre-recur T1ce scans overlaid with warped recurring ROI are shown on the top left, followed by the SVM_{PE} predictions on the bottom left, and the other four sequences (T1, T2, FLAIR, and ADC) on the right. Colors from blue to red encodes an increased pseudo recurrent risk from 0 to 1.

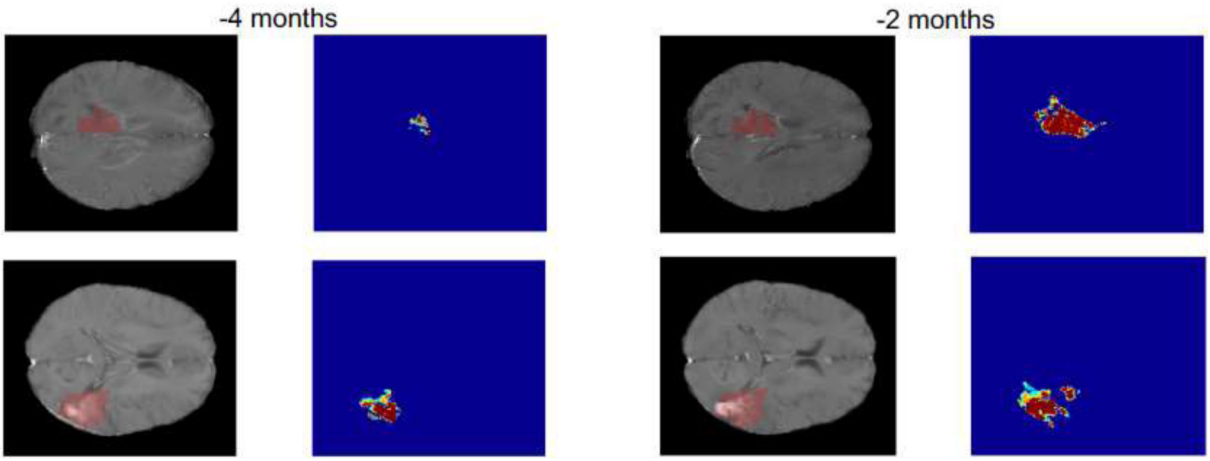

Figure 4:

Visualization of SVM_{PE} predictions on the 4-month (two columns on the left) and 2-month (two columns on the right) pre-recur time points for 4 example subjects. SVM predictions are shown next to the corresponding T1ce scan from the same time point for all patients. Warped recurrences are shown in red and overlaid on the T1ce scans. Colors from blue to red encodes an increased pseudo recurrent risk from 0 to 1.

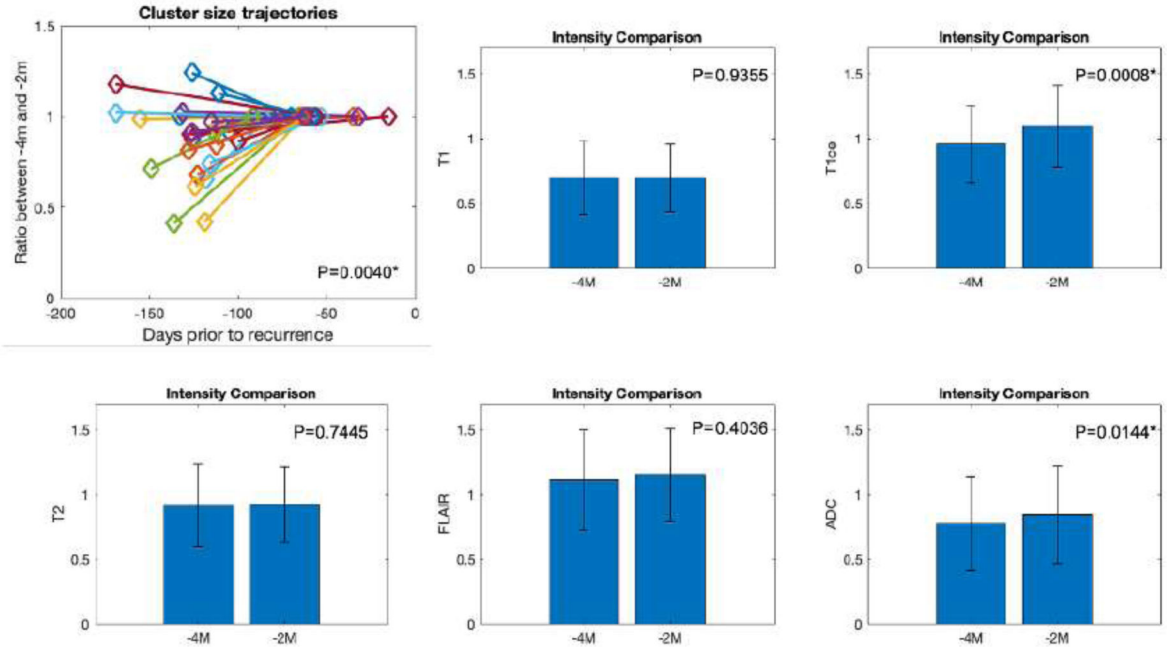

Figure 5:

Results of exploratory comparisons between two pre-recur time points on SVM_{PE} predictive cluster size, as well as 5 MR image intensities within recurrence ROIs. Statistically significant ($p < 0.05$) differences between the two time points were detected in cluster sizes, T1ce intensities, and ADC values.

Table 1:

Performance evaluation metrics of SVM_{PE} on the 2-month pre-recur dataset. For both the training and testing datasets, four metrics (Recall, Precision, F1 score, and ABD) are presented, along with their corresponding group-wise comparison p-values. No statistically significant ($p < 0.05$) differences were detected on the four metrics between the discovery and testing sets.

	Training*		Testing		P-values
	Mean	**SD**	**Mean**	**SD**	
Recall	**0.81**	**0.13**	**0.80**	**0.10**	**0.591**
Precision	**0.68**	**0.14**	**0.69**	**0.14**	**0.684**
F1	**0.73**	**0.12**	**0.73**	**0.10**	**0.978**
ABD (mm)	**8.14**	**6.33**	**7.49**	**6.19**	**0.722**

* For the training dataset, performance scores are reported after 10-fold cross-validation.